

PREPRINT: Expert decision support system for aeroacoustic classification

A. Goudarzi,^{1, a} C. Spehr,^{1, b} and S. Herbold^{2, c}

¹German Aerospace Center (DLR), Germany

²Karlsruhe Institute of Technology (KIT), Germany

This paper is part of a special issue on Machine Learning in Acoustics.

This paper presents an expert decision support system for time-invariant aeroacoustic source classification. The system comprises two steps: first, the calculation of acoustic properties based on spectral and spatial information; and second, the clustering of the sources based on these properties. Example data of two scaled airframe half-model wind tunnel measurements is evaluated based on deconvolved beamforming maps. A variety of aeroacoustic features are proposed that capture the characteristics and properties of the spectra. These features represent aeroacoustic properties that can be interpreted by both the machine and experts. The features are independent of absolute flow parameters such as the observed Mach numbers. This enables the proposed method to analyze data which is measured at different flow configurations. The aeroacoustic sources are clustered based on these features to determine similar or atypical behavior. For the given example data, the method results in source type clusters that correspond to human expert classification of the source types. Combined with a classification confidence and the mean feature values for each cluster, these clusters help aeroacoustic experts in classifying the identified sources and support them in analyzing their typical behavior and identifying spurious sources in-situ during measurement campaigns.

©2022 Acoustical Society of America. [<https://doi.org/DOI number>]

[XYZ]

Pages: 1–16

I. INTRODUCTION

Multiple noise-generating phenomena and mechanisms exist in aeroacoustics^{6,13}. To identify these phenomena in measurements, expert domain knowledge and a detailed study of measurements are necessary. For the localization and estimation of the sound power of complex aeroacoustic sources, beamforming is a reliable method¹¹. Beamforming results in high dimensional maps of the Power Spectral Density (PSD) that are difficult and time-consuming to analyze manually. Therefore, the resulting beamforming maps are usually integrated over space and frequency areas to obtain low-dimensional data such as spectra¹⁰ which human experts then analyze, classify, and interpret. For the classification of the sources experts often rely upon the spatial localization and meta-information, e.g., that sources are located at a cavity and thus, are identified as cavity noise. In real-world scenarios, this information can be missing or misleading, since the geometries of interest, such as planes, trains, and cars, are highly complex and result in a superposition of sound generating mechanisms. Thus, classifying aeroacoustic sources is a complex, time-consuming task that forces experts

to build comprehensive databases based on simplified, generic, and controlled measurements that may not reflect the behavior of real-world sources.

The goal of this paper is to enable the identification and classification of sound sources based on their acoustic properties alone. Machine learning is a powerful tool that currently outperforms any other automated classification system given enough learning data^{4,9}. Since not enough classified data is available to employ supervised machine learning, we use unsupervised learning techniques to identify clusters of similar sources or source mechanisms from acoustic source spectra. These clusters help experts to identify sound source types, classify them based on their acoustic properties, and detect typical and anomalous behavior without having to rely on spatial or meta-information.

To cluster the sources, the information contained in their spectra has to be condensed and transformed to a machine-interpretable feature-space. To do so, we identify and define characteristic features that formalize expert knowledge to enable the automated calculation of acoustic properties. The presented method is built on the fundamental assumption that the physical source mechanisms can be determined by the observation of their source spectra over increasing Mach number. Thus, the features are defined to be independent of the

^aarmin.goudarzi@dlr.de

^bcarsten.spehr@dlr.de

^csteffen.herbold@kit.edu

absolute Mach number. As a result, the features are comparable for measurements, that are performed at different Mach numbers, which enable the clustering of sources from multiple measurement campaigns together.

For this paper, we use deconvolved beamforming maps of the scaled air-frame models of a Dornier 728 (Do728)² and an Airbus A320 (A320)³ as example data to derive these features, discuss their usefulness, and specify a proof-of-concept implementation. We employ the Source Identification based on spatial Normal Distributions (SIND)⁵ approach to identify aeroacoustic sources and obtain their spectra from the beamforming maps. Since there is no ground-truth for the datasets, we present our manual evaluation of the airframe source types with exemplary source spectra and our decision choices to the reader. These source types are mostly distinguishable in the introduced feature-space and unsupervised learning methods show clustering choices that correlate to our manually evaluated source types. However, for some source types, the clustering differentiates them into multiple clusters which may indicate that there are further sub-types. In other cases, multiple source types are grouped together, which indicates that these may be sub-types of an unknown super-type. Thus, the clustering result provides suitable guidance and supports experts in the identification of source types.

II. DATASETS

TABLE I. Measurement matrix of the Do728 dataset.

$\langle \text{Re} \rangle_M [1 \times 10^6]$	1.4	1.8	2.5	3.8	10.6
$T[\text{K}]$	290	250	200	150	100
$p_0 [1 \times 10^5 \text{ Pa}]$	1	1	1	1	1

The data used in the present paper consists of beamforming measurements of two closed-section wind tunnel models: one is of a Do728² and one is of an A320³. Both models were observed at various angles of attack, various Mach numbers and several Reynolds numbers. For the Do728 model, the Mach averaged Reynolds numbers $\langle \text{Re} \rangle_M$, the ambient pressures p_0 and cryogenic temperatures T are shown in table I based on the mean aerodynamic cord length $D_0 = 0.353 \text{ m}$. Values of $\alpha_i = [1^\circ, 3^\circ, 5^\circ, 6^\circ, 7^\circ, 8^\circ, 9^\circ, 10^\circ]$ were chosen for angle of attack for every mean Reynolds number and $M_i = [0.125, 0.150, 0.175, 0.200, 0.225, 0.250]$ as Mach number for every measurement configuration. The array consisted of 144 microphones at an aperture of $1.756 \text{ m} \times 1.3 \text{ m}$ and a data sample frequency of $f_S = 120 \text{ kHz}$ was used.

TABLE II. Measurement matrix of the A320 dataset.

$\langle \text{Re} \rangle_M [1 \times 10^6]$	1.4	5.1	5.1	19.9
$T[\text{K}]$	310	311	125	120
$p_0 [1 \times 10^5 \text{ Pa}]$	1.10	3.99	1.15	4.19

The A320 model was observed at $\alpha_i = [3^\circ, 7^\circ, 7.15^\circ, 9^\circ]$ for every mean Reynolds number, and $M_i = [0.175, 0.200, 0.225]$ for every measurement configuration. The mean Reynolds numbers, the ambient pressures p_0 and cryogenic temperatures T are shown in table II based on $D_0 = 0.353 \text{ m}$. The array consisted of 96 microphones at an aperture of $1.06 \text{ m} \times 0.5704 \text{ m}$ and the data was recorded at $f_S = 150 \text{ kHz}$. Thus, the Do728 dataset contains a total of 240 measurements and the A320 contains 48 measurements. The Cross-Spectral density Matrices (CSM) were calculated using Welch's method with a block size of 1024 samples with 50% overlap. The beamforming was performed using conventional beamforming¹¹ and CLEAN-SC deconvolution¹⁷ on a regular grid with a focus point resolution of $\Delta x_1 = \Delta x_2 = 5 \times 10^{-3} \text{ m}$. The acoustic source positions and Region Of Interests (ROI) were automatically detected using the SIND method⁵.

III. METHODOLOGY

An aeroacoustic source emerges either from the interaction of an obstacle placed in a flow, e.g., a cylinder¹⁹ or from the flow itself, e.g., jet noise⁷. When we observe a source at a specific flow speed or angle of attack, the observed acoustic source is often a realization of one or more underlying physical mechanisms. These mechanisms often depend monotonously on parameters such as the Mach or Reynolds number. To distinguish between different source mechanisms, we have to identify the underlying parameters for which the source mechanism is self-similar. The observable variables depend on the measurement matrix, in controlled wind tunnel experiments. They can be the angle of attack α , wind speed u , Mach number M , temperature T , and ambient pressure p_0 . The variation in pressure and temperature changes the Reynolds number, the variation of u and T changes the Mach number M . Wind tunnel facilities often use scaled models, increased pressures, and a lowered temperature to achieve high, real-world Reynolds numbers². For these flow variations, the source's ability to radiate acoustic energy to the far-field can be observed with beamforming, which is described by the source emission power, quantified by the Power Spectral Density (PSD)¹¹. Thus, the result of beamforming in wind tunnels is a high-dimensional sound power map $\text{PSD}(\vec{x}, f, M(T, u), \alpha, \text{Re}(T, u, p_0))$.

A basic assumption in aeroacoustic source modeling is that small changes in subsonic Mach numbers do not

alter the source mechanism⁶. Also, a source may exist in extended spatial areas or frequency intervals, e.g., the generated sound from vortices in Kármán’s vortex street^{14,19}. Sources may shift their peak frequencies with increasing Mach number and their location over frequency. An example is jet noise where with increasing Mach number the dominant sound generation location moves downstream and the peak frequency decreases, while the PSD level increases⁷. Thus, increasing the Mach number can change the sound power or shift peak frequencies and the source location, but a normalization of the PSD or frequency by the Mach number reveals that the spectrum shape, normalized peak frequencies and normalized PSDs coincide. Therefore, the underlying physical sound-generating mechanism has not changed, we only observe a different realization of the source mechanism. However, source mechanisms can change completely for high variations of their Reynolds numbers, e.g., the radiated acoustics from a flow around a cylinder¹⁹, where the flow properties suddenly change, e.g., the transition from a laminar to a turbulent flow. All other variations such as the angle of attack α or changes in geometry may alter the dominant source mechanism abruptly (e.g., slat tones and flow separation in airframe noise may appear). We treat these variations as potentially different source mechanisms.

Since we are interested in classifying the sources according to their underlying physical mechanisms rather than classifying them by their dominance, we need to analyze the scaling behavior over Mach number and similarity laws⁶ rather than absolute levels at specific Mach numbers. Thus, a sound source has the free variables PSD (\vec{x}, f, M) at a fixed $\langle \text{Re}_0 \rangle_M$ and α_0 . For example, a source that was identified by SIND in a ROI (\vec{x}_i) of the Do728 dataset is treated as a unique source for each angle of attack and Reynolds number (which results in $8\alpha_0 \times 5\text{Re}_0 = 40$ individual sources), each represented by six spectra at different Mach numbers $M_i = [0.125, \dots, 0.250]$. This allows us to extract features from the source spectra, which are Mach normalized representations of the sources. Since we assign multiple spectra of measurements at different Mach numbers to one source, we can derive its acoustic properties not only from the individual spectra but from the changes over Mach number or as an average property of the spectra. This has the advantage, that the Mach-normalized features of different datasets are comparable despite their measurement at different Mach numbers. Additionally, the averaging reduces relative errors.

However, this method has two limitations. First, the aeroacoustic properties always depend on the Reynolds number, which itself linearly depends on the flow speed. Thus, when increasing the flow speed at constant pressure or temperature, the Reynolds number increases. As discussed above, a change in Reynolds number may change the source mechanism. Often, this is not a prob-

lem since the acoustic properties do not change drastically over multiple orders of magnitude of the Reynolds number⁶. As we show in Section VI A, the variation of the Reynolds number normally results in a drift of the Strouhal number with increasing Mach number. We introduce a normalized frequency which is a generalization of the Strouhal and Helmholtz number, which accounts for this drift. Consequently, we neglect the change in Reynolds number caused by the change in Mach number and assume a Mach averaged mean Reynolds number for the sources. Second, the source mechanisms can also vary fundamentally with Mach number, especially under trans- and supersonic conditions, even at constant Reynolds number, e.g., jet screech¹⁵. Therefore, we solely focus on small, subsonic Mach number changes. Still, the source spectra presented in this paper suggest that many source mechanisms exhibit a small dependency on subsonic Mach number changes.

IV. PROCEDURE

The proposed expert decision support system consists of four steps, which we discuss in detail in the subsequent sections.

1. The preprocessing and preparation of acoustic source spectra at different Mach numbers, see section V.
2. The calculation of features that describe the source mechanism, see section VI.
3. The clustering of the sources based on the features, see section VIII.
4. The manual analysis and labeling of the source clusters based on mean feature values and expert knowledge.

V. SPECTRA PREPARATION

The proposed expert decision support system is based on the feature calculation from source spectra. We obtain these spectra either from single source measurements or from measuring multiple sources at the same time with beamforming¹¹ using either manually defined ROIs or using automatic source identification methods such as SIND⁵. For the data presented in this paper, we use SIND to obtain the source positions and source spectra.

A. Spectra interpolation

We apply a preprocessing step before calculating features based on the spectra: the spectra are interpolated onto a logarithmic Strouhal and Helmholtz frequency vector. Thus, a discrete bin of the frequency vector represents a constant frequency interval ratio. This ensures that each frequency interval is equally weighted for the calculation of the corresponding features. Also, we will compare spectra over Strouhal and Helmholtz number

bin-wise, which requires interpolation to align the frequency bins at different Mach numbers.

B. Source spectra separation

Source spectra can exhibit multiple different source mechanisms in different frequency intervals, either because of complex source mechanisms or simply because a ROI or single measurement contained multiple sources that are super-positioned in the spectra. To calculate correct features based on which the sources can be clustered, we first need to separate the sources which feature multiple mechanisms into sub-sources that only contain the corresponding partial spectrum. This step has to be carried out before the feature calculation, so the feature-set presented in this paper cannot be used to detect this behavior. Thus, we focus on an easily detectable characteristic that many source spectra with multiple mechanisms exhibit. We found that often, a spectrum scales at low frequencies over Strouhal number and at high frequencies over Helmholtz number or vice versa. Thus, there exist two different aeroacoustic mechanisms. We use this observation in the following to identify and separate the spectra accordingly.

Consequently, we cut each source spectrum into two sub-spectra and calculate the mean broadband self-similarity (see subsection [VIB](#)) for four cases:

1. For the Strouhal number at low and high frequencies.
2. For the Strouhal number at low and the Helmholtz number at high frequencies.
3. For the Helmholtz number at low and the Strouhal number at high frequencies.
4. For the Helmholtz number at low and high frequencies.

Figure 1 c) shows the resulting mean self-similarity for different cut-frequencies for a slat / slat track source of the Do728. We calculate the Strouhal number cut-frequency using the mean Mach number $St = He / \langle M_i \rangle$. The global optimum of the four cases defines the optimal cut frequency and the frequency types of the sub-spectra. In this case, we achieve the optimal self-similarity when we use the Strouhal number at low frequencies (Figure 1 a, below the vertical black line) and the Helmholtz number at high frequencies (Figure 1 b above the vertical black line). However, often it is not clear (even for a human) if the spectrum should be separated and a false positive separation has a greater impact on the feature calculation and clustering than a false negative separation. Hence, we prefer to leave a spectrum intact if the need for separation is unclear. We define a variety of rules that must be met before the source is separated into sub-sources. First, the overlapping spectra at different Mach numbers must cover at least two octaves to prevent small sub-spectra with little information. Second, the sub-spectra should both cover at least half an

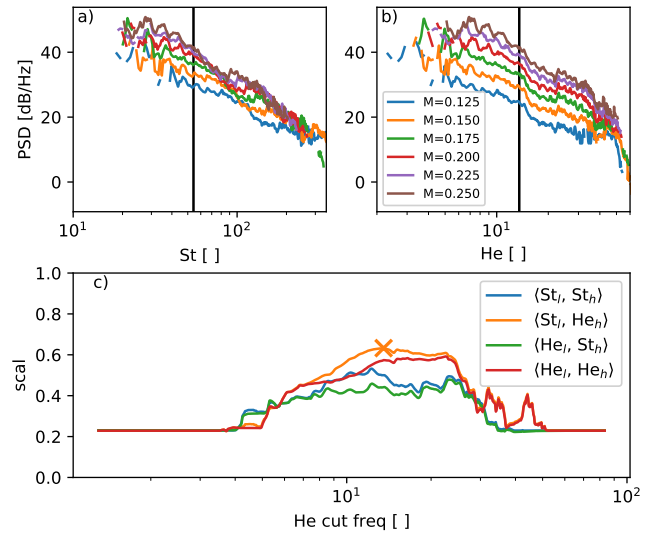


FIG. 1. (Color online) Do728, $Re = 1.4 \times 10^6$, slat / slat track source at $\alpha = 1^\circ$. a) shows the spectra over Strouhal and b) over Helmholtz number. The vertical black lines depict the optimal frequency to separate the spectra into low l and high h sub-spectra, to ensure their optimal self-similarity. In c) the mean self-similarity (scal), see eq. 6, for the four possible combinations of Strouhal $St_{l,h}$ and Helmholtz number $He_{l,h}$ based on the depicted spectra cut-frequency on the x-axis are shown. The x marks the global maximum, which leads to the spectra separation in a) and b). For this source, a Strouhal number scaling below $He \approx 15$ and Helmholtz number scaling above this frequency achieves the optimal self-similarity of the sub-spectra.

octave to prevent small, irrelevant spectra parts. Third, we only separate the source if the optimal similarity is achieved using a different scaling behavior at low and high frequencies. Forth, the mean self-similarity of the sub-spectra of different frequency-types must feature at least a 10% improvement over the maximum mean self-similarity of the same frequency types. In the example of the slat / slat track, the first three rules are met, but the self-similarity improvement of around 7% from $He_{cut}(\langle St_l, He_h \rangle) \approx 14$ would not justify the spectrum separation, compared to sub-spectra with a Helmholtz number scaling at $He_{cut}(\langle He_l, He_h \rangle) \approx 24$. The parameters for the rules are based on the presented data and can be adjusted to meet a more or less rigorous separation policy.

VI. FEATURE ENGINEERING

We require a set of features that describe the aeroacoustic properties of a source based on their spectra. A feature-set must meet the following conditions:

- All features together must unambiguously describe a source or its mechanism.

- A feature must describe a basic property of a source and must provide additional information.
- The calculation of a feature must be automatable.
- A feature must be represented by a single numerical value.
- A feature must correspond to a physical property.

As the procedure is intended to support the expert, the last condition is necessary to enable the interpretation of the results. We identified the following aeroacoustic properties which are broken down to numerical features in the subsequent sections:

- The frequency normalization exponent, see sub-section [VIA](#).
- The broadband self-similarity, see sub-section [VIB](#).
- The sound power scaling, see sub-section [VIC](#).
- The tonality, see sub-section [VID](#)
- The source location dependency on the Mach number, see sub-section [VIE](#)
- The spatial source distribution, see sub-section [VIF](#).
- The spectrum shape, see sub-section [VIG](#).

A. Frequency normalization exponent

An important property of any aeroacoustic source is the self-similarity or scaling behavior scal_f over increasing Mach number. An acoustic spectrum that exhibits self-similarity over the Strouhal number indicates a physical source mechanism that is connected to the flow such as turbulence-induced noise⁷. With the speed of sound a the Strouhal number is defined as

$$\text{St} = \frac{fD_0}{Ma}. \quad (1)$$

Spectra collapsing over the use of Helmholtz number

$$\text{He} = \frac{fD_0}{a}. \quad (2)$$

indicate a mechanism connected to acoustic resonances¹³ or radiation effects¹². We observed in the presented data that Strouhal-scaling spectra do not perfectly align over the Strouhal number. In this rare case of multiple cryogenic measurement conditions, both datasets allowed us to observe spectra at constant Reynolds number over increasing Mach number (at decreasing temperatures and increasing pressure). With the dynamic viscosity $\mu(T)$ and density $\rho(p_0, T)$ of the medium, the Reynolds number is

$$\text{Re} = \frac{\rho(p_0, T)M(T, u)D_0}{\mu(T)}. \quad (3)$$

At a constant Reynolds number, the spectra aligned perfectly over the Strouhal number at increasing Mach number. We observed, that the increase of Reynolds number over Mach number at constant pressure and temperature

causes sources to decrease or increase their frequency dependency on the Mach number. Since cryogenic measurements are rare and expensive, we assume that many datasets are observed at constant pressure and temperature and are affected by this phenomenon. Thus, we define a modified normalized frequency \hat{f} that always allows a collapse of the spectra by introducing the generalized frequency normalization exponent m with

$$\hat{f} = \frac{fD_0}{M^{m_a}}. \quad (4)$$

Note that this normalized frequency is a generalization of the Helmholtz number (for $m = 0$) and the Strouhal number (for $m = 1$), so if $m \geq 0.5$ we will speak of a modified Strouhal number. To obtain the generalized frequency normalization exponent, we optimize the collapse of the spectra using the definition of the broadband self-similarity (see Section [VIB](#)). Figure 2 shows the comparison of the *a*) normal Strouhal number and *b*) the modified Strouhal number with $m = 0.72$. Figure 2 *c*) shows the mean spectra correlation (black line) over the modification exponent and the standard deviation 1σ as a gray area. The blue line is the mean p-value $\langle p \rangle_M$, indicating the reliability of the correlation estimation. The optimal value for m (shown with the red x) is achieved at the global maximum of the self-similarity, see equation 6, which is a combination of the mean Pearson correlation coefficient of the spectra at different Mach numbers, its standard deviation, and its mean p-value. If a spectrum is dominated by a Helmholtz number scaling mechanism, the frequency modification exponent will result in values $m \approx 0$. Since we will present spectra always over both Helmholtz and (modified) Strouhal number, we have to find a local maximum of the self-similarity function around $m \approx 1$ to account for spectra that include a minor, Strouhal number scaling mechanism. To do so, we run a standard peak detection over the self-similarity function $\text{scal}_f(m)$ to find a local maximum $m \geq 0.5$. If none is found and $m < 0.5$, we simply choose $m = 1$ for the (modified) Strouhal number.

The following acoustic properties are derived from the spectra, which can be displayed over the Strouhal number, the Helmholtz number, or the introduced generalized frequency. There are two possible methods for the calculation of features based on normalized frequency spectra. Either we calculate the features only based on spectra scaled over the generalized frequency, or we calculate the features independently over both the modified Strouhal number and the Helmholtz number. The disadvantage of the first method is that the results depend heavily on the correct determination of the frequency modification exponent. As described in sub-section [VB](#), spectra can feature multiple frequency regions with different self-similarities. To calculate the correct frequency modification exponent, we must separate the spectra beforehand. Since the spectra separation approach is based on the broadband self-similarity, (see Section [VIB](#)) which requires a correct modified frequency exponent, this ap-

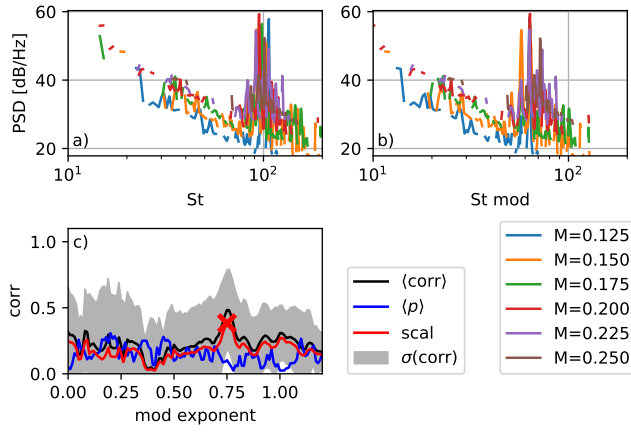


FIG. 2. (Color online) Do728, $Re = 1.4 \times 10^6$, slat tones at $\alpha = 8^\circ$. Comparison of source spectra at different Mach numbers over *a*) normal Strouhal number and *b*) modified Strouhal number, see eq. 4, with $m = 0.74$. *c*) shows the mean and standard deviation σ of the Pearson correlation coefficient of the source spectra at different Mach numbers over the variation of the modification exponent, the mean p -value, the resulting self-similarity (scal), see Section VI B. The modification exponent $m = 0.74$ achieves the optimal self-similarity, marked with an x .

proach must be performed by iteration and thus, is not very robust. Also, aeroacoustic experts are used to analyzing spectra displayed over Strouhal and Helmholtz number. Additionally, we prefer a reliable method even if the expert decides not to separate any spectra. Thus, we focus on the second approach, i.e. we calculate features from spectra displayed over both Helmholtz and modified Strouhal number separately, because they might contain parts that scale over one or the other.

B. Broadband self-similarity

As stated in sub-sections VB and VIA a spectrum scales either over the modified Strouhal or the Helmholtz number. If these source spectra are self-similar over one of these frequency types, there is a linear dependency between the PSD levels over frequency at different Mach numbers. Thus, we calculate the Pearson correlation coefficients $\rho_{i,j}$ between all spectra at different Mach numbers M_i and M_j .

$$\text{corr}_k = \rho_{i,j}(\text{PSD}(M_i, f), \text{PSD}(M_j, f)) \quad \text{for } i > j \quad (5)$$

Often, the mean correlation $\langle \text{corr}_k \rangle_k$ exhibits multiple local maxima and thus, is not an optimal definition for the self-similarity. However, it can be improved by taking its standard deviation $\sigma_k(\text{corr}_k)$ and the mean p -value $\langle p_k \rangle_k$ into account. Due to the beamforming process in combination with CLEAN-SC, the discrete spectra often contain missing values. If we drop these frequency bins before the calculation, the standard deviation σ , and the p -value p will increase drastically when the spectra are

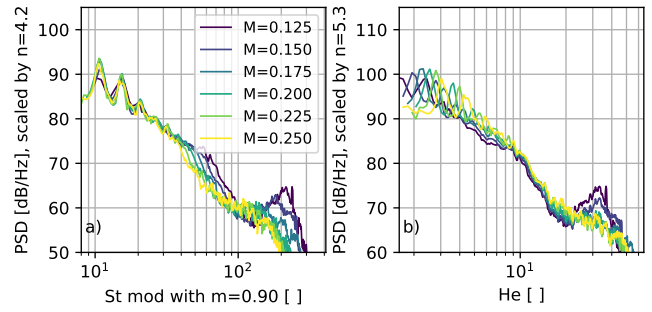


FIG. 3. (Color online) Do728 slat / slat track source at $Re = 1.4 \times 10^6$, $\alpha = 3^\circ$. Comparison of the power scaling over modified Strouhal ($m = 0.9$) and Helmholtz number to collapse the PSDs with eq. 7. The scaling exponents are $n_{St} = 4.2$, $n_{He} = 5.3$, $n_{OASPL} = 6.3$.

not aligned properly. Using these properties, we introduce the final broadband self-similarity (scal)

$$\text{scal} = (\langle \text{corr}_k \rangle_k - \sigma_k(\text{corr}_k)) (1 - \langle p_k \rangle_k). \quad (6)$$

Figure 2 *c*) shows the mean correlation coefficient and its standard deviation, the mean p -value and the resulting self-similarity for a slat tone source over a variety of modification exponents m .

C. Sound power scaling

The power of aeroacoustic noise generally increases with increasing Mach number. A prominent example is jet noise for which Lighthill derived the M^8 scaling law⁷. Thus, when doubling the Mach number, the PSD will increase by $10 \log_{10}(2^8) = 24$ dB. The power scaled PSDs ($\widehat{\text{PSD}}$), with the power scaling exponent n , are given by

$$\widehat{\text{PSD}}(f, M_j) = \text{PSD}(f, M_j) - n 10 \log_{10}(M_j). \quad (7)$$

Conventionally, a regression on the Overall Sound Pressure Levels (OASPL, which is the sound power integrated over frequency) or peak levels of eq. 7 is used to determine n . This does not work properly for spectra from beamforming maps, since the microphone array aperture in combination with CLEAN-SC acts like a low-cut filter in absolute frequency. This is especially problematic when scaling over the Strouhal number (and Helmholtz number when scaling spectra at different temperatures and pressures) because this results in a Mach number dependent low-cut frequency and thus, in a wrong scaling exponent. To avoid this problem, we minimize the mean distance between all power scaled spectra $\widehat{\text{PSD}}(f_i, M_j)$ over frequency bin-wise with a standard bounded minimization algorithm. To calculate the mean distance between multiple spectra at once we use the standard deviation σ of the PSDs at every frequency bin. Since parts of a spectrum with a high level are often considered more important for the scaling, we can weigh the standard deviations at every frequency bin with the mean spectrum

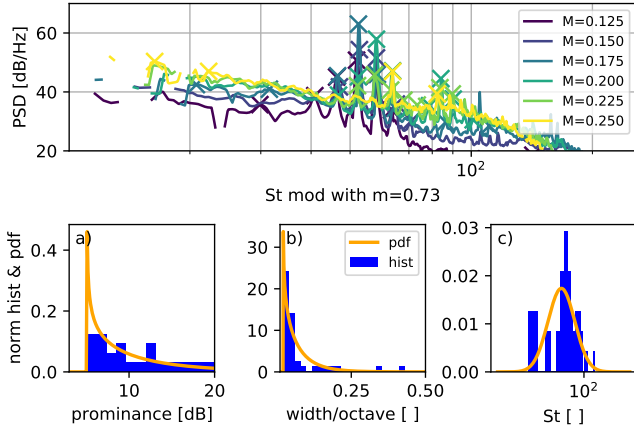


FIG. 4. (Color online) Do728, $Re = 1.4 \times 10^6$, slat tones at $\alpha = 8^\circ$. Top, the spectra and the automatically detected peaks, depicted with an x . Bottom, a normalized histogram and the fitted PDF of the *a*) peaks prominence, *b*) peak width, and *c*) peak Strouhal number.

power $\langle \text{PSD}(f_i, M_j) \rangle_{M_j}^\gamma$ with $\gamma \geq 0$. The weighting exponent γ determines by how much we want to prefer the scaling of high levels. Thus, we minimize

$$\min_{0 \leq n < \infty} \sum_{f_i} \left[\sigma_j \left(\text{PSD}(f_i, M_j) - n 10 \log_{10}(M_j) \right) \langle \text{PSD}(f_i, M_j) \rangle_j^\gamma \right], \quad (8)$$

with $n, \gamma \in \mathbb{R} \geq 0$. For the calculation of a reliable power scaling exponent at least spectra at three different Mach numbers should be used. A large variation in Mach number also increases the scaling's reliability. Figure 3 shows the resulting power scaling for a slat / slat track source and $\gamma = 10$ over modified Strouhal number and Helmholtz number. Note the different scaling behavior over Strouhal and Helmholtz number for the low and high-frequency part of the spectrum and that the OASPL scaling neither matches the Helmholtz nor the Strouhal scaling exponent correctly, as described above. In Figure 6 more examples of scaled PSDs with $\gamma = 10$, which was used for all sources presented in this paper, are displayed.

D. Tonality

Accounting for the tonal behavior of the sources is a complex task and results in less straightforward feature descriptions, since the number of tonal peaks P varies from source to source and within a source for different Mach numbers but we have to define a constant amount of feature values that describe their properties. These properties are the peak-width interval P_w , the peak prominence P_p , the peak frequencies P_f , and the number of peaks P_n . We also want to know whether the peaks scale well over the modified Strouhal or Helmholtz

number ($\text{scal}_{p,f}$). First, we run a standard automated peak detection over the spectra. The number of peaks P_n is a straightforward value, and we take their average number from the spectra at different Mach numbers.

$$\widehat{P}_n = \langle P_n(M_j) \rangle_j \quad (9)$$

As stated in section VI, we have to break down the properties of the peaks to single value features. We do so by describing the distribution of the peaks instead of using the individual peaks' properties directly. Naturally, peaks with lower prominence appear more often than peaks with very high prominence. This assumption is also used for the peak width. This behavior can be modeled using a gamma distribution¹. With the gamma function $\Gamma(k)$, the Probability Density Function (PDF) γ of the gamma distribution over x with a shape k , scale θ and location l is

$$\gamma(x, k, \theta, l) = \frac{(x-l)^{k-1} \exp(-\frac{x-l}{\theta})}{\theta^k \Gamma(k)} \quad \text{for } x, k, \theta \geq 0. \quad (10)$$

For the peak frequency locations, we found that a log-normal distribution fits most of the sources best. The distributions of these properties have unknown shape (standard deviation), scale (distribution median), and location (distribution offset) parameters which can be approximated from any number of samples greater than one by fitting the gamma or log-normal distribution to the data with standard fitting methods. The slope, scale, and location for each the peak width, peak prominence, and peak frequencies are used as comparable feature values, independent of the number of tones in the PSDs and the number of different Mach numbers. Figure 4 shows the peak detection and the corresponding distributions for all Mach numbers of a Do728 slat tone source. We set a lower threshold of 3 dB for the peak prominence to prevent the algorithm from detecting lots of irrelevant low-level peaks which dominate the distributions. We set the feature values to zero if only one or less tones are detected.

To determine how well the prominent peaks scale over Strouhal or Helmholtz number we average the ratio of how many peaks overlap at every detected peak frequency interval. Working on discrete logarithmic frequency bins f_i , we introduce two sets. A_i are the sets of Mach numbers which feature a peak $P_w(M_j)$ at the corresponding frequency bin f_i . B is the single set of unique frequency bins f_i for which at least one spectrum $\text{PSD}(M_j)$ features a peak $P_w(M_j)$.

$$A_i = \{M_j \mid \text{so that } f_i \in P_w(M_j)\} \quad (11)$$

$$B = \{f_i \mid \exists M_j \text{ so that } f_i \in P_w(M_j)\} \quad (12)$$

The resulting scaling of the tones is then the ratio of spectra that share a peak at the same frequency bin to the total number of spectra at different Mach numbers $|M_j|$, averaged over all frequency bins i for which at least

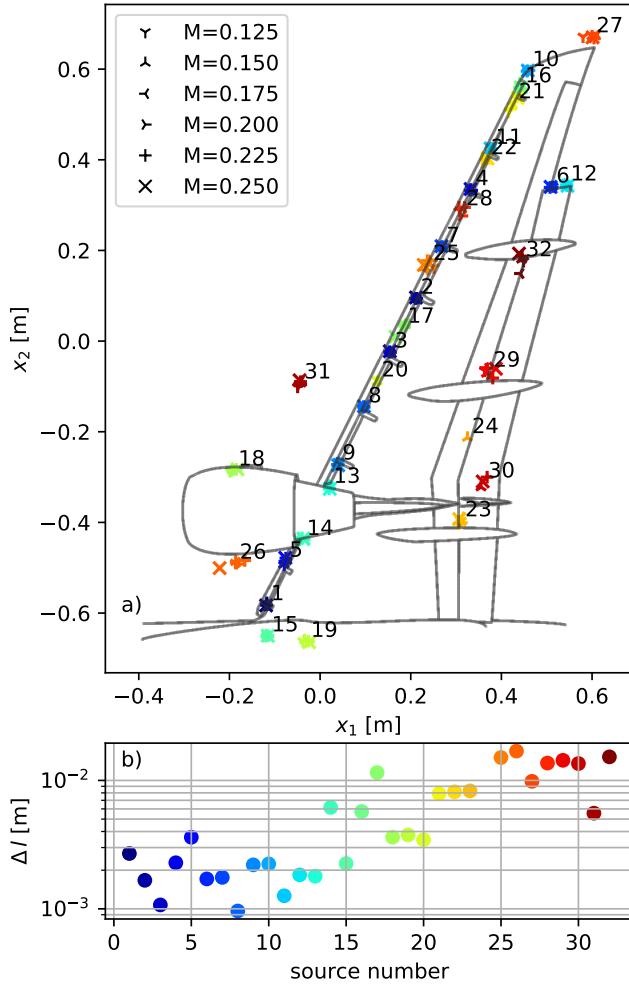


FIG. 5. (Color online) Do728. *a*) shows the source positions at $Re = 1.4 \times 10^6$, $\alpha = 10^\circ$ (if the source is present at this configuration) for the given Mach numbers. *b*) shows the mean movement of the sources calculated with eq. 15.

one peak was detected

$$\text{scal}_{p,f} = \left\langle \frac{|A_i| - 1}{|M_j| - 1} \right\rangle_i. \quad (13)$$

The minus ones ensure a soft feature value $0 \leq \text{scal}_{p,f} \leq 1$ for the modified Strouhal and Helmholtz number, since each A_i contains at least one element. Again, if A is empty (no peaks exist, thus, they do not scale) we set $\text{scal}_{p,f} = 0$. Finally, we introduce the tonal proportion prop_p , defined as the Mach averaged ratio of tonal SPL to total SPL. It expresses how much percent of the energy in the spectra is caused by tones.

$$\text{prop}_p = \left\langle \frac{\sum_i \text{PSD}(f_i \in B, M_j)}{\sum_j \text{PSD}(f_i, M_j)} \right\rangle_j. \quad (14)$$

E. Source location dependency on the Mach number

The spatial location of some aeroacoustic sources may change with the Mach number. An example of a moving source would be a flow detachment, at which the sound generating eddies move further downstream with increasing Mach number or jet noise, while cavity noise would remain at the same location. Figure 5, top, shows the variation of source positions on the Do728 with increasing Mach number. For a numeric feature description, we calculate the positional change of the source with increasing Mach number and call it the source movement. We define the source movement Δl as the mean movement of the local source position \vec{x} , normalized by the change in Mach number, shown in Figure 5, bottom. A limitation of this feature is that it assumes the monotonous movement of the source in one direction with the Mach number.

$$\Delta l = \left\langle \frac{|\vec{x}_j - \vec{x}_{j-1}|}{M_j - M_{j-1}} \right\rangle_j \quad \text{for } j \geq 2 \quad (15)$$

F. Spatial source distribution

Aeroacoustic sources can be spatially distributed, such as line or volume sources. We use the sources' spatial PDFs obtained with SIND to describe this behavior. SIND approximates the spatial source distributions with 2D normal distributions, described by the standard deviations σ_{x_i} . We define the integrated, normalized PDF area A as a feature for the spatial expansion of the source distribution.

$$A = \int_{x_1} \int_{x_2} \text{PDF}(x_1, x_2) dx_2 dx_1 \quad (16)$$

We define the ratio of the PDFs standard deviations σ_{x_i} as an indicator for line sources with

$$R = \max \left(\frac{\sigma_{x_1}}{\sigma_{x_2}}, \frac{\sigma_{x_2}}{\sigma_{x_1}} \right). \quad (17)$$

Thus, $R \approx 1$ indicates a point or sphere-like source while an increasing R indicates a line source.

G. Spectrum shape

To capture the general spectrum shape, we use a linear regression $L(f)$ for $\text{PSD}(f)$ which consists of two values: the interception b of the line at $f = 0$ Hz and the slope a

$$L(f) = af + b. \quad (18)$$

The interception is an absolute value, varies with the Mach number, and is, therefore, discarded. The slope is the increase or decrease of the PSD level over the frequency. Additionally, we use the regression's r^2 -value which describes how well the linear regression explains the spectrum. A low r^2 value indicates that the linear regression is not capturing the movement in the spectrum well. Thus, it is an indication of the waviness of

the spectra.

Similar to the spatial source distribution, we define a source distribution over frequency. Since we work on sparse spectra which are not defined on all frequency bins, we use the mean f_{mean} and standard deviation f_{std} of the existing frequencies to capture in which frequency interval the source exists. With the sets C_j that contain the defined frequency bins f_i for the spectra at Mach number M_j

$$C_j = \{f_i \mid \text{so that } \text{PSD}(M_j, f_i) \neq \text{NaN}\} \quad (19)$$

the

$$f_{\text{mean}} = \langle C_j \rangle_j \quad (20)$$

$$f_{\text{std}} = \sigma_j(C_j) \quad (21)$$

VII. MANUAL DATA CLASSIFICATION

As a first step, we manually identify source categories and label the sources in the presented datasets accordingly, which enables us to analyze and quantify the results of the presented method. We note that the classification and label choice may be ambiguous, contain errors, and misinterpretations, since we mostly rely on the spatial appearances of the sources for the labels. Additionally, we analyzed the spectra of every single source in the datasets to identify sub and super-categories. To make this process transparent to the reader, we present in Figure 6 exemplary Do728 spectra for the most common categories. Note that sources in the left column are displayed over the modified Strouhal number and sources in the right column are displayed over the Helmholtz number.

- The slats feature Strouhal number scaling peaks with overtones that decay in level and prominence with increasing frequency, see Figure 6 a). They are located between the slat tracks.
- The slat track noise scales over Helmholtz number, see Figure 6 b). At high frequencies it often exhibits a Helmholtz scaling hump that is Mach number dependent.
- The slat tones feature extremely dominant Strouhal number scaling small-band tones, see Figure 6 c). They are mainly located at the slat positions.
- The flap (track) tones feature a small Helmholtz scaling tone, see Figure 6 d).
- The trailing flap side edge features a prominent Strouhal scaling peak, see Figure 6 e).
- The leading flap side edge features a smaller Helmholtz scaling peak, see Figure 6 f). At increasing Reynolds numbers, a second Helmholtz number scaling peak emerges.
- The strake noise is a Strouhal number scaling hump, see Figure 6 g). It increases in intensity with increasing angle of attack and disappears with increasing Reynolds number.

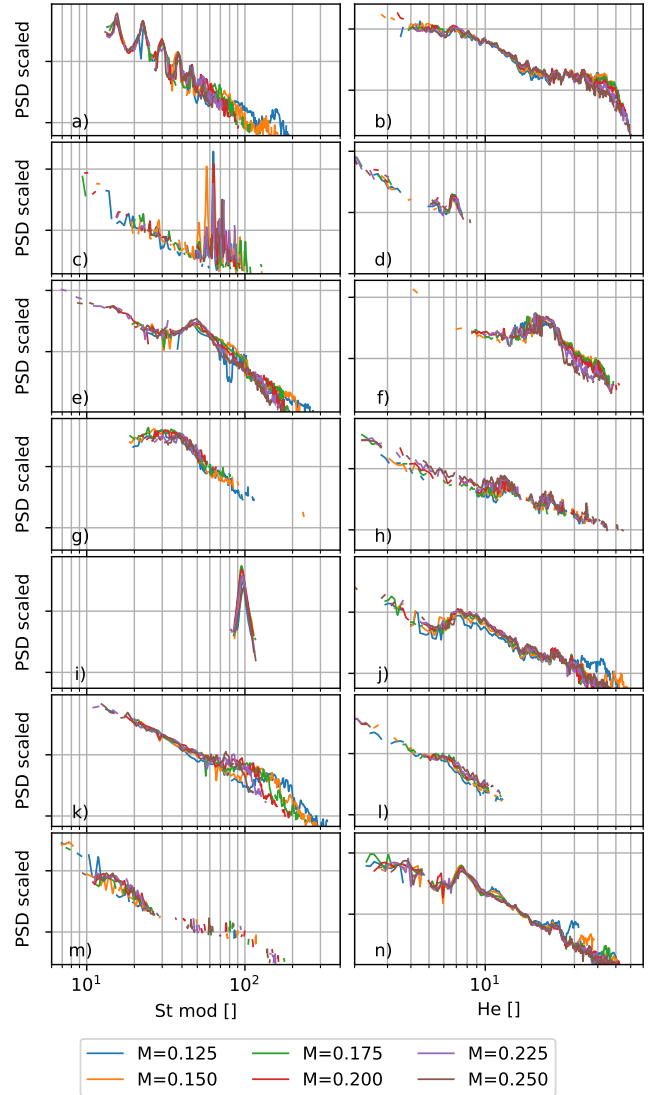


FIG. 6. (Color online) Do728, normalized spectra of the typical source types: a) slat with $m = 0.90, n = 4.44$, b) slat track with $n = 5.47$, c) slat tone with $m = 0.75, n = 3.43$, d) flap tone with $n = 4.23$, e) trailing flap side edge with $m = 1.09, n = 4.43$, f) leading flap side edge with $n = 4.09$, g) strake at low Reynolds number and high angle of attack with $m = 0.71, n = 3.43$, h) wind tunnel with $n = 3.87$, i) strake tone at high Reynolds number and low angle of attack with $m = 0.94, n = 3.68$, j) outer nacelle with $n = 5.47$, k) slat edge with $m = 1.00, n = 3.26$, l) flap track with $n = 6.07$, m) wing tip with $m = 0.66, n = 3.59$, and n) slat resonance with $n = 6.26$. The horizontal grid lines depict $\Delta 20$ dB.

- The wind tunnel noise scales over Helmholtz number, see Figure 6 h). It appears next to the wing and is considered as a spurious noise source in this measurement².
- The strake tone is a dominant Strouhal scaling tone, see Figure 6 i). It appears only at high

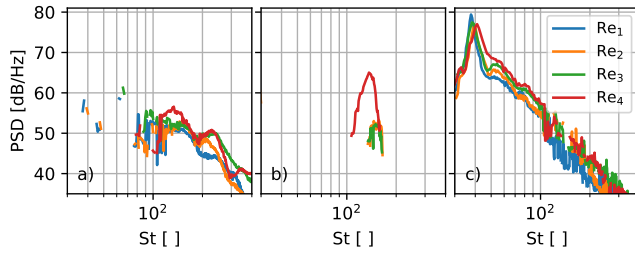


FIG. 7. (Color online) A320. The figure shows the Reynolds number effect on the source types *a*) leading flap side edge at $\alpha = 7^\circ$, $M = 0.175$, *b*) high Strouhal number scaling tone at $\alpha = 9^\circ$, $M = 0.200$, located on the slat and flap, and *c*) trailing flap side edge at $\alpha = 7^\circ$, $M = 0.200$.

Reynolds numbers and low angles of attack and decreases in intensity with increasing angle of attack.

- The outer nacelle area features a broadband hump that scales over Helmholtz number, see Figure 6 *j*).
- The slat edge is located close to the wing tip and its noise scales over Strouhal number, see Figure 6 *k*). The spectrum level decays over frequency and features an additional, low-level Helmholtz scaling hump at high frequencies.
- The flap track noise features a low-level Helmholtz number scaling hump, see Figure 6 *l*).
- The wing tip noise features a Strouhal number scaling hump, see Figure 6 *l*), that increases in intensity with increasing angle of attack. The spectra are often contaminated with wind tunnel noise.
- The slat (track) resonance exhibits strong, Helmholtz number scaling peaks, see Figure 6 *n*).

The fuselage, nacelle track, inner slat gap, and flap gap are identified and named based on their spatial appearance. A noise occurring at the flap gap was caused by loose tape on the model during the measurement. Additionally, the category slat / slat track is introduced to account for various spectra that are located on the slat tracks but ambiguous, e.g. the slat / slat track shown in Figure 1, containing some Strouhal number scaling low frequencies and some Helmholtz number scaling high frequencies.

The manual classification of the A320 dataset is much more challenging. The smaller microphone array results in less reliable spectra, especially at low frequencies, and due to the small variation in Mach number the correct scaling behavior and scaling exponent are difficult to identify. Additionally, the typical spectra do not consistently correlate with the spatial appearance of the sources, e.g. the spectra are different for different flap tracks. Finally, the sources are strongly affected by the shift in Reynolds number which often results in sources that are transitioning from one mechanism to another. Thus, there are multiple sources that share

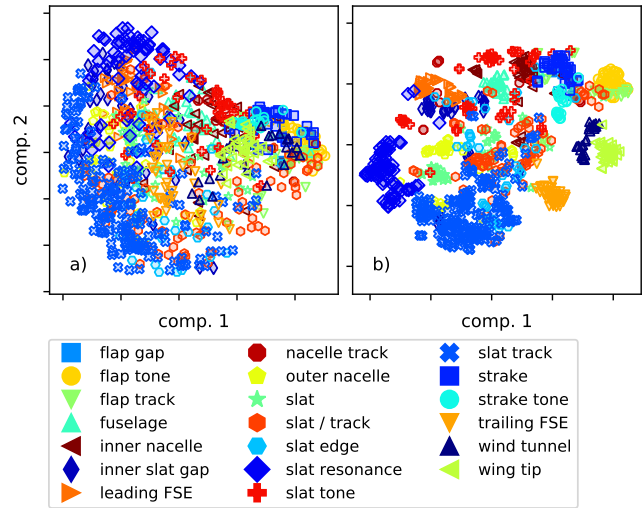


FIG. 8. (Color online) Do728. Shows the first two feature components of *a*) KPCA with RBF kernel which will be used for clustering and *b*) a TSNE for visualization purposes.

the same label, but feature different spectra (e.g., the fuselage, the slat tracks, and leading flap side edge, see Figure 7 *a*)) and vice versa. In addition to the Do728 source types, there exist multiple sources on the slat and flap that feature a high Strouhal number scaling tone (high St tone) that increases in intensity with increasing Reynolds number like the strake tone, see Figure 7 *b*). Also, with increasing Reynolds number the peak frequency of the slat, the slat tone, the strake and the strake tone decreases (with a St mod exponent of $m \approx 0.7$) while it increases for the trailing flap side edge ($m \approx 1.1$), see Figure 7 *c*).

We visualize the labeled sources in their feature-space to determine if the features are suitable to distinguish between different source types and mechanisms. We perform two projection techniques on the feature-space to display as much information in two dimensions as possible: 1) a Kernel Principal Component Analysis (KPCA)¹⁶ with a Radial Basic Function (RBF) as kernel which will be later used for clustering; 2) a t-Distributed Stochastic Neighbor Embedding (TSNE)¹⁸. Figure 8 shows the results for the Do728. We observe that the sources form separable blobs based on the manually proposed categories by distance and distribution density. Note, the features do not include the source location, the Reynolds number, the angle of attack or any absolute SPL information. This suggests that sources with the same source mechanism have similar feature distributions, so they are closer to each other in introduced feature-space compared to sources with a different source mechanism.

We can also observe how similar the source types are based on the distance in their feature-space. Often,

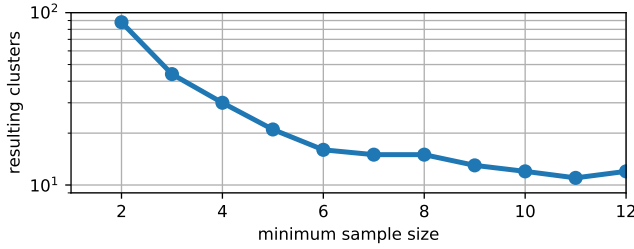


FIG. 9. (Color online) Do728, the figure shows the resulting numbers of clusters from HDBSCAN over the minimum sample size parameter.

the spurious wind tunnel noise polluted to wing tip spectra and they both feature a low-level, low-frequency hump (with a different scaling behavior) and thus, they are very close in the TSNE projection. The slat tracks and slat resonance blobs are close, but distinct which correlates to our evaluation. We also observe how the slat tracks overlap with the slat / slat track category and finally merges with the slats. Generally, on the bottom left of Figure 8 b) we find sources that scale over Helmholtz number, on the top right sources scale over Strouhal number.

VIII. SOURCE CLUSTERING

To overcome the manual classification challenges, we showed in sub-section VII we use unsupervised clustering techniques that group the sources based on their acoustic properties alone. Thus, the clustering has no knowledge of the Reynolds numbers, the angles of attack, and the source positions. We select Hierarchical Density-Based Spatial Clustering of Applications with Noise (HDBSCAN)⁸, which supports soft clustering without prior knowledge about the number of clusters, i.e., the number of different source types, and a clustering confidence. We normalize the features prior to the clustering and perform a KPCA as mentioned before, which retains $2\sigma \approx 95\%$ of the information by discarding feature dimensions with little variance. HDBSCAN requires a minimum sample size which determines how many source members a cluster must have below which it is discarded. We can determine a reasonable sample size by examining their resulting cluster numbers. With an increasing sample size, the resulting quantity of clusters first drops massively and then decreases only slightly, see Figure 9 for the Do728 dataset. We pick the sample size after which the total quantity of clusters n_{clusters} only decreases slightly, in this case around $n_{\text{samples}} = 7$. We call the procedure for this expert decision support system “Clustering sources based on their aeroacoustic features” (CRAFT).

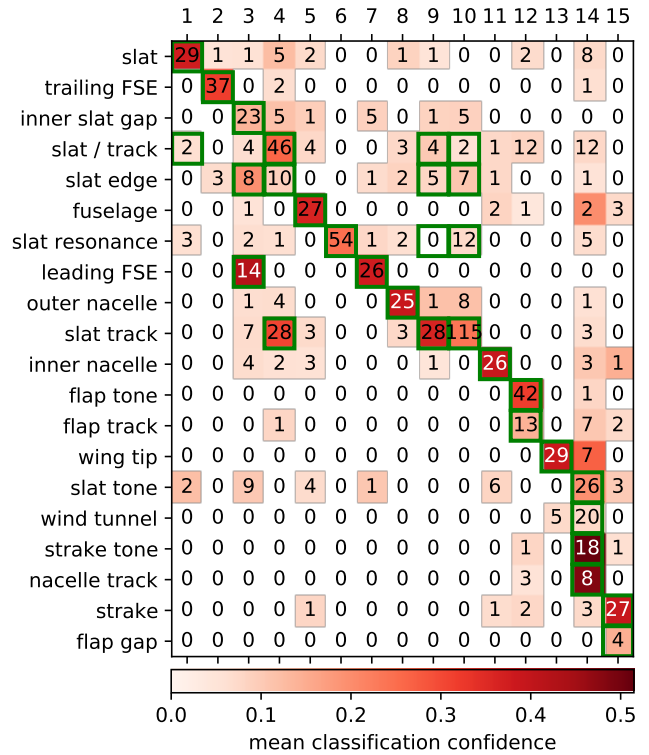


FIG. 10. (Color online) Do728, confusion matrix of the SIND and CRAFT classification process that quantifies how often a source with the corresponding label was clustered to the corresponding cluster number. The color intensity displays the mean clustering confidence. The correct cluster choices are marked with a box.

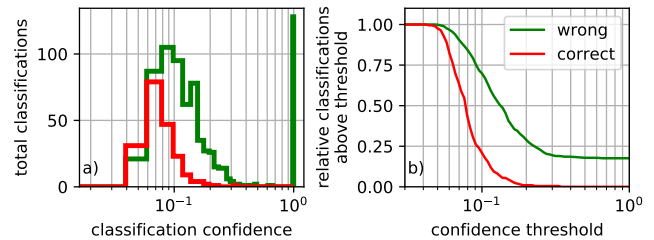


FIG. 11. (Color online) Do728, a) shows a histogram of total wrong and correct cluster choices over their classification confidence. b) shows the relative number of cluster choices above the confidence threshold t_C on the x -axis.

IX. RESULTS

The results presented are based the Do728 and A320 datasets, obtained from sparse beamforming maps with SIND and processed with CRAFT. For the Do720, a minimum sample size of seven was used for HDBSCAN. CRAFT determined fifteen source clusters. Figure 10 shows a confusion matrix of the manually determined labels, see sec. VII, and the clustering results. The matrix

shows how often a source from a manually determined category was clustered into the corresponding clusters. Given the manual source classification is correct, a perfect clustering would result in a cluster group for every manual label and all corresponding sources would be clustered within their corresponding group. Thus, a perfect clustering would achieve a square confusion matrix with all results on the diagonal. The underlying color in the confusion matrix depicts the mean clustering confidence. Since most clusters correlate to the manual labels (they are mostly located on the diagonal axis), our definition of correct clustering results (which are marked with a green box in the confusion matrix) will be based on its comparison to the manual labels.

To identify the clusters which correspond to the manual labels we will take the occurrence of source types per cluster, their estimated confidence, and their similarity to other source types into account. Thus, cluster number one is assigned to the slat sources. Slat sources assigned to cluster one are considered correct, slat sources assigned to other clusters are considered wrong. A slat resonance which was categorized as cluster number nine or ten (which consist mainly of slat tracks) instead of cluster number six (which consists solely of slat resonances) is considered correct, since it is a sub-type of a slat track source. All sub-categories that are clustered with their super-categories are considered correct, but not vice versa. Thus, slat tracks that are classified as cluster six (slat resonances, a sub-category of slat tracks) are considered wrong. Slats and slat tracks that fall in the cluster four (slat / slat track) and vice versa are considered correct, which is a super-category of these ambiguous sources. Cluster numbers three, four, fourteen and fifteen comprise multiple source types. As long as the corresponding source types were classified as the cluster that contained most of the sources, they are considered correct. The slat tracks occupy the two clusters number nine and ten with a high clustering confidence, which we consider as equally correct. The same holds true for the leading flap side edge in cluster number three and seven. All other classifications are considered as wrong. The usefulness of the chosen clusters can only be evaluated qualitatively, based on their consistency and ability to separate source types or source mechanisms.

In total, 213 out of 928 Do728 source predictions (23.95%) are considered wrong and 715 (77.04%) are considered correct. Figure 11 a) shows the confidence of the clustering choices. Both, the correct and wrong clustering choices decrease with increasing confidence. Figure 11 b) shows the relative number of wrong and correct clustering choices that lie above the classification confidence threshold t_C . We observe that the number of wrong classifications decreases much more rapidly than the number of correct classifications. As an example, if the clustering choices with a confidence below $t_C = 0.1$ are discarded, only a prediction for 59.26% of the

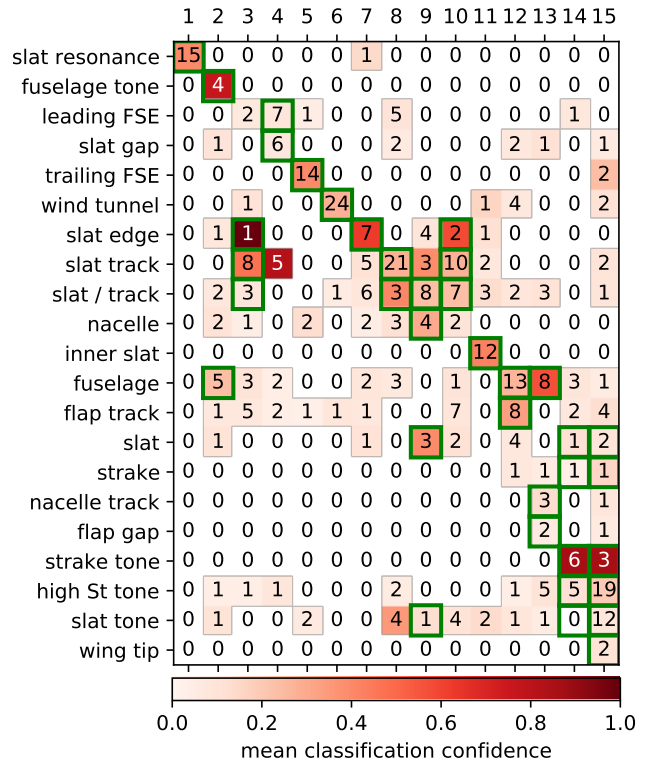


FIG. 12. (Color online) A320, confusion matrix of the SIND and CRAFT classification process that quantifies how often a source with the corresponding label was clustered to the corresponding cluster number. The color intensity displays the mean clustering confidence. The correct cluster choices are marked with a box.

sources is retained, but the prediction accuracy increases to 91.45%.

Figure 12 shows the confusion matrix of our labels and the classification results for the A320. The correct clusters are determined as stated above for the Do728. In total, 157 out of 408 source predictions (38.48%) are wrong and 251 (61.52%) are correct. As shown for the Do728 classification, if the clustering choices with a confidence below $t_C = 0.1$ are discarded, only a prediction for 58.58% of the sources is retained, but the prediction accuracy increases to 72.80%.

X. DISCUSSION

We presented the expert decision support system CRAFT and evaluated its results on two datasets, based on CLEAN-SC beamforming maps of two similar scaled airframe models in closed wind tunnel sections. CRAFT was built on the assumption that an aeroacoustic source is driven by a mechanism that reveals its nature over the variation of the Mach number. Thus, we used spectra measured at different Mach numbers to determine the

source’s aeroacoustic properties. The limitation of this general assumption is that we neglected any changes of the source mechanism over the Mach number. We saw in Figure 1 b) at high Helmholtz numbers and in Figure 2 b) that the sources can exhibit a substantial Mach dependency, which is not captured by the proposed method. The advantage of this assumption is that the properties are defined independently of the employed Mach numbers, which allows the clustering of data from different measurement configurations.

In sub-section VB we showed that spectra often contain frequency intervals, that are governed by different physical mechanisms. While we observed most of the characteristic features at lower Strouhal numbers $St \leq 100$, some sources showed a different behavior at high Strouhal numbers, see Figure 3. For this, we identified the inner slat, slat / slat tracks, slat edge and the nacelle vicinity, see Figure 1, Figure 3, and Figure 6 a), j), k) and n). We showed that this behavior can be detected using the definition of the self-similarity over Strouhal and Helmholtz number from sub-section VIB. We assumed that if a spectrum scales at low frequencies over Strouhal number and at high frequencies over Helmholtz number or vice versa, it must be governed by two different source mechanisms. Thus, the source spectra can be separated into sub-spectra that feature a single source mechanism, respectively. Since a false positive separation of a spectrum can lead to the insufficient calculation of aeroacoustic properties we introduced rules to ensure a conservative spectrum separation policy. The variables of these rules were based on the spectra of the presented datasets and should be reviewed for other data. The sources in our data showed mostly one or two different frequency regions, but more complex sources might be possible. Since we had to manually classify all individual sources for a ground truth and interpret the clustering results, we chose not to complicate the process by splitting spectra. However, the clustering results may be improved using this technique.

Some properties depended on the employed normalized frequency, e.g., to calculate the power scaling exponent, we need to know if the spectra scale over Helmholtz or Strouhal number, see Figure 3. In sub-section VIA, we presented a method on how to determine the correct normalized frequency, given that a single mechanism governs the source spectra. However, we decided to calculate all features that are frequency-dependent over both the Helmholtz and the Strouhal number independently and let the clustering algorithm decide which information is relevant. This approach proved to be robust towards insufficient spectra separations or the insufficient prediction of the frequency type. Additionally, the procedure is intended to support aeroacoustic experts which are already used to display spectra over both the Helmholtz and the

Strouhal number.

In sub-section VIA we showed that the normal Strouhal number definition is not sufficient when working with source spectra at different Reynolds numbers. Since $Re \propto M$ at constant temperature and ambient pressure, the Reynolds number typically increases with increasing Mach number within a measurement configuration. To account for this, we introduced a normalized frequency that is a generalization of the Strouhal and Helmholtz number by implementing the modification exponent m . The traditional Strouhal number is $m = 1$ and the Helmholtz number $m = 0$. We found for noise that is related to the slat or slat tones at $Re = 1.4 \times 10^6$ a modification exponent of $m \approx 0.76 \pm 0.08$ and for the trailing flap side edge $m \approx 1.10 \pm 0.02$. Since at low temperatures the increase in Reynolds number over Mach number is stronger, we also observe stronger drifts of the modification exponent. Due to the small sample size of Reynolds number configurations, the underlying dependency of $m(\partial Re)$ could not be determined. However, the present data suggest a non-linear and source mechanism dependent relationship.

To evaluate the quality of CRAFT, we classified the presented datasets manually. Due to the beamforming and spectra reconstruction process, many spectra were degenerated, with missing and insufficient information, e.g., the inconsistent peaks at low Strouhal numbers in Figure 1. Additionally, we showed in Figure 7 that sources can gradually shift their spectrum shape with increasing Reynolds number. Thus, we heavily relied on meta-information for the classification such as the source position. Since the proposed method was designed to overcome exactly this problem, the resulting metrics should be evaluated with caution.

To enable the automatic clustering of the data, we presented multiple aeroacoustic properties in section VI which we translated into a numeric feature-space. The properties were selected to capture common aeroacoustic concepts and to explain the different spectra types in the presented datasets. We proposed formulas for the features with the main goal of robustness during their automated calculation. We neither claim that the list of the properties is complete and covers all acoustic phenomena nor do we claim that the feature calculation is robust in all data scenarios. We hope to spark a discussion in the aeroacoustic community on which properties are important for which source types, how these can be broken down to numeric feature values and how they can be calculated in a robust and efficient way.

The feature distributions varied greatly for the manually labeled source types. We assume the reason for this are the degenerated spectra, the fact that many spectra are a combination of different source mechanisms, and that the quantity of source type members varies greatly. We observed this in the feature projection in Figure 8

b), where the slat tracks were scattered over the map and bridged multiple other source clusters. Nevertheless, many of our manually classified Do728 source types were separable in their feature-space, independently of their location, angle of attack, Reynolds number, or SPL. This suggests that the proposed feature-space included enough information to separate multiple source types and mechanisms.

The goal of the presented expert decision support system CRAFT was to analyze new, complex data in a scientific context. Consequently, we used unsupervised learning techniques to identify source types with similar acoustical properties instead of supervised learning techniques. We chose HDBSCAN⁸ since it allowed us to cluster the data without any prior assumption of the expected number of source types or source distributions in the feature-space. It also provided soft clustering, which estimated the probability for each source of belonging to each cluster. In combination with the mean feature values of each cluster, which directly correspond to aeroacoustic properties, this should allow the expert to transparently analyze the clustering choices.

For the Do728, CRAFT resulted in very intuitive clusters similar to our manual evaluation (see Figure 10). If the feature variance within a class became too large (e.g., the slat tracks or leading flap side edge), we often found multiple clusters that represent a single label class. This can be caused by differences in their spectra, which again result from different flow properties, geometric differences, source directivities, or source identification artifacts. It can also be caused by the imbalance of label members in the dataset. Since our own classification was often ambiguous and since not all clusters related to our labels the exact accuracy of CRAFT is up for debate. Our evaluation of the clustering was based on the confusion matrix in Figure 10 and resulted in an accuracy of 77.04 %.

The usefulness of the chosen clusters can only be evaluated qualitatively, based on their ability to separate source mechanisms from each other and detect sources for which the spatial location is misleading. For airframe noise, typical analyzed source regions are the whole slat, flap, flap side edge, and nacelle region, including the strakes^{2,3}. Regarding the slat region, CRAFT showed that typical slat sources (cluster number one) are distinctly different from slat track sources (core cluster numbers nine and ten). Occasionally, slat tones (cluster number 14) appeared with decreasing probability towards high Reynolds numbers. Often, they were at the same source position, but at different angles of attack (slat noise appeared mainly at low angles of attack). CRAFT was able to separate these phenomena very well. On the contrary, CRAFT clustered sources at different spatial locations to the single cluster number fourteen. When we reviewed the corresponding source spectra it became clear that this cluster represents sources that

feature Strouhal number scaling tones (at a low Strouhal modification exponent of $m = 0.844 \pm 0.147$).

For the A320, CRAFT's clusters often did not correlate well to our manual classification (which is not necessarily a bad thing) and thus, the accuracy of the result was much more difficult to evaluate. The evaluation was based on the confusion matrix in Figure 12 and resulted in an accuracy of 61.52 %. Again, the usefulness of the chosen clusters is evaluated qualitatively. In the slat area, CRAFT correctly determined different clusters for the slat sources, the slat tracks, the inner slat, the slat tones, and the slat resonances. These were all sources with distinctly different spectra. When reviewing the source clusters fourteen and fifteen we observed that both featured sources with Strouhal number scaling tones. However, they can be separated in strong, high SPL tones in cluster fourteen, e.g. the high Reynolds number spectrum in Figure 7 b), and weak tones in cluster fifteen, e.g. the low Reynolds number spectra in Figure 7 b). When reviewing the soft cluster confidences for sources in cluster number 14, they featured also very high confidence for cluster number fifteen and vice versa. Thus, CRAFT predicted reasonable sub-categories for Strouhal number scaling tones. The same holds true for the slat resonances, which also features high confidence of belonging to the slat track clusters.

Many clusters proved to be meaningful representations of source categories. While the underlying physical mechanisms, the correct labels and thus, CRAFT's accuracy is up for debate, the clustering was mostly consistent between the Do728 and A320 dataset, which featured similar source types. We showed that CRAFT worked on the very large Do728 dataset with 928 individual sources, consisting of six spectra each, and the relatively small A320 dataset with 408 sources, consisting of three spectra each.

XI. CONCLUSION

The goal of this paper was to use unsupervised learning techniques to cluster multiple sources based on their aeroacoustic properties to reveal underlying physical mechanisms and guide the acoustic expert in classifying and analyzing the sources correctly. The general assumption of this expert decision support system "CRAFT" was that the physical mechanism of a source can be determined by its spectrum change over Mach number. Thus, source measurements at multiple flow speeds were required. We used the method "SIND" to automatically detect aeroacoustic sources of a Dornier 728 and an Airbus A320 in CLEAN-SC beamforming maps and extract their corresponding spectra.

To reduce the complex acoustic properties to a data space that can also be understood by the machine, we introduced a feature-set that expresses these properties as a combination of single, numerical values. These

features are independent or averaged over the spectra at different Mach numbers, which enables CRAFT to compare and cluster sources from different experiments. To further evaluate the data, we presented exemplary source spectra and a manual classification approach for the sources based on their spatial appearance and spectral features. We showed that the manual labeling of the sources is often ambiguous due to degenerated spectra, multiple source mechanisms, or Reynolds number dependent trends which resulted in additional uncertainty. Despite the ambiguous manual classification, many source categories formed distinguishable distributions in the introduced feature-space. However, especially the large population of slat tracks showed a large variance in their spectra and feature values and consequently connected multiple other source distributions.

We used the HDBSCAN algorithm to cluster the sources in the introduced feature-space which did not include meta-information such as the source position, the angle of attack, or the Reynolds number. The cluster selection was meaningful, consistent between the datasets, and provided the necessary information to identify sources that behaved atypically for their spatial locations. For example, it allowed the correct identification of multiple source types that were all located on the slat. The result also provided a confidence estimation for the clustering results. We showed that sources are mostly misclassified by CRAFT at low confidence, while the clustering with high confidence is usually correct. Experts can discard predictions below a confidence threshold which further increases the prediction accuracy.

Being able to quickly analyze sources and build labeled datasets this way has many advantages. It enables the reliable analysis of source-type dependent features such as the power scaling with a mean and a standard deviation. Since the presented features are independent of the absolute Mach number, CRAFT also enables the comparison of different models measured in different wind tunnels at different flow configurations. Since the analysis is run within minutes instead of typically weeks or months for datasets of the presented sizes, CRAFT can also be used to detect spurious sources in-situ during experiments.

For future work we plan to analyze more data with the introduced method to further evaluate the quality and reliability of the proposed features. We also hope to start a discussion in the aeroacoustic community on the selected properties and their corresponding features, possible shortcomings, alternative definitions or calculation methods, and the classification of aeroacoustic source phenomena.

ACKNOWLEDGMENTS

We want to thank the experts of the aeroacoustic group Göttingen, especially Dr. Thomas Ahlefeldt, for the helpful discussions on the analyzed beamforming results. The authors also acknowledge the DLR, Institute of Aerodynamics and Flow Technology, Department of Experimental Methods (contact: Carsten Spehr) for providing the SAGAS software which generated the beamforming and CLEAN-SC results for this paper.

- ¹Abramowitz, M. (1974). *Handbook of Mathematical Functions, With Formulas, Graphs, and Mathematical Tables*, (Dover Publications, Inc.).
- ²Ahlefeldt, T. (2013). “Aeroacoustic measurements of a scaled half-model at high reynolds numbers,” *AIAA Journal* **51**(12), 2783–2791, doi: [10.2514/1.J052345](https://doi.org/10.2514/1.J052345).
- ³Ahlefeldt, T. (2017). “Microphone array measurement in european transonic wind tunnel at flight reynolds numbers,” *AIAA Journal* **55**(1), 36–48, doi: [10.2514/1.J055262](https://doi.org/10.2514/1.J055262).
- ⁴Bianco, M. J., Gerstoft, P., Traer, J., Ozanich, E., Roch, M. A., Gannot, S., and Deledalle, C. A. (2019). “Machine learning in acoustics: Theory and applications,” *The Journal of the Acoustical Society of America* **146**(5), 3590–3628, doi: [10.1121/1.5133944](https://doi.org/10.1121/1.5133944).
- ⁵Goudarzi, A., Spehr, C., and Herbold, S. (2021). “Preprint dummy: Automatic source localization and spectra generation from sparse beamforming maps,” *The Journal of the Acoustical Society of America*.
- ⁶Howe, M. S. (2007). *Hydrodynamics and Sound* (Cambridge University Press).
- ⁷Lighthill, M. J., and Newman, M. H. A. (1952). “On sound generated aerodynamically i. general theory,” *Proceedings of the Royal Society of London. Series A. Mathematical and Physical Sciences* **211**(1107), 564–587, doi: [10.1098/rspa.1952.0060](https://doi.org/10.1098/rspa.1952.0060).
- ⁸McInnes, L., Healy, J., and Astels, S. (2017). “hdbscan: Hierarchical density based clustering,” *The Journal of Open Source Software* **2**(11), doi: [10.21105/joss.00205](https://doi.org/10.21105/joss.00205).
- ⁹Mello, R. F., and Ponti, M. A. (2018). *Machine Learning* (Springer International Publishing).
- ¹⁰Merino-Martinez, R., Sijtsma, P., Rubio Carpio, A., Zamponi, R., Luesutthiviboon, S., Malgoezar, A., Snellen, M., Schram, C., and Simons, D. (2019). “Integration methods for distributed sound sources,” *International Journal of Aeroacoustics* **18**, 1475472X1985294, doi: [10.1177/1475472X19852945](https://doi.org/10.1177/1475472X19852945).
- ¹¹Merino-Martínez, R., Sijtsma, P., Snellen, M., Ahlefeldt, T., Antoni, J., Bahr, C. J., Blacodon, D., Ernst, D., Finez, A., Funke, S., Geyer, T. F., Haxter, S., Herold, G., Huang, X., Humphreys, W. M., Leclère, Q., Malgoezar, A., Michel, U., Padois, T., Pereira, A., Picard, C., Sarradj, E., Siller, H., Simons, D. G., and Spehr, C. (2019). “A review of acoustic imaging methods using phased microphone arrays,” *CEAS Aeronautical Journal* **10**(1), 197–230, doi: [10.1007/s13272-019-00383-4](https://doi.org/10.1007/s13272-019-00383-4).
- ¹²Michalke, A. (1977). “On the effect of spatial source coherence on the radiation of jet noise,” *Journal of Sound and Vibration* **55**(3), 377–394, doi: [https://doi.org/10.1016/S0022-460X\(77\)80020-5](https://doi.org/10.1016/S0022-460X(77)80020-5).
- ¹³Müller, E.-A., ed. (1979). *IUTAM Symposia Mechanics of Sound Generation in Flows* (Springer-Verlag Berlin Heidelberg).
- ¹⁴Prandtl, L., and Tietjens, O. (1957). *Applied hydro and aeromechanics* (Dover).
- ¹⁵Raman, G. (1999). “Supersonic jet screech: Half-century from powell to the present,” *Journal of Sound and Vibration* **225**(3), 543 – 571, doi: <https://doi.org/10.1006/jsvi.1999.2181>.
- ¹⁶Schölkopf, B., Smola, A., and Müller, K.-R. (1998). “Non-linear component analysis as a kernel eigenvalue problem,” *Neural Computation* **10**(5), 1299–1319, doi: [10.1162/089976698300017467](https://doi.org/10.1162/089976698300017467).

¹⁷Sijtsma, P. (2007). "Clean based on spatial source coherence. international journal of aeroacoustics," International Journal of Aeroacoustics **6**, doi: [10.1260/147547207783359459](https://doi.org/10.1260/147547207783359459).

¹⁸van der Maaten, L. J. P., and Hinton, G. (2008). "Visualizing high-dimensional data using t-sne," Journal of Machine Learning Research .

¹⁹Zdravkovich, M. M. (1997). *Flow around circular cylinders*, **1** (Oxford university press).